

## **CubeSat Dual-axis Solar Array Articulation**

AME 441 - Senior Design Lab - Group 22

Elle Barker, Derek Chibuzor,  
Yahir Garcia, Didi Abdel Rhim

6 September - 11 December 2024

### **1. Abstract**

CubeSats exist at the forefront of cost-effective academic research and broadening industrial applications in space. To support the progress of research and space exploration using these uniquely compact, easily launched vehicles, power generation methods must develop beyond current industry standards. Current CubeSat missions have occasionally underperformed their projected life cycles due to insufficient on-orbit power generation, a drawback that is entirely preventable. One method to improve CubeSat resilience and broaden their space applications involves increasing the complexity of their solar array configuration. Beyond more passive systems like a body-fixed or static deployed system, single and dual-axis articulation systems could dramatically extend CubeSat lifespans and allow for more demanding missions. The modeled CubeSat experiment detailed in this report explored the voltage output from a simple solar panel housing capable of simulating all four solar array configurations: body-fixed, statically deployed, single-axis articulation, and dual-axis articulation. A significant improvement over the single-axis articulation along the pitch axis was observed with the dual-axis articulation system along pitch and yaw, with a voltage output increase of  $42 \pm 7\%$ . While the articulating systems were expected to significantly outperform the passive configurations, some flaws in the experimental method resulted in comparable performance between the static deployed configuration and the dual-axis articulation system.

## 2. Introduction

### 2.1 History

CubeSats were invented in 1999 by professors at California Polytechnic State University and Stanford University, intending to provide a useful instructional tool for their students' comprehension of basic satellite construction [1]. They are a standardized class of nanosatellites, ranging from the original 1U, a cube with 10 cm long sides shown in Figure 1, and scaling at increments of 1U.

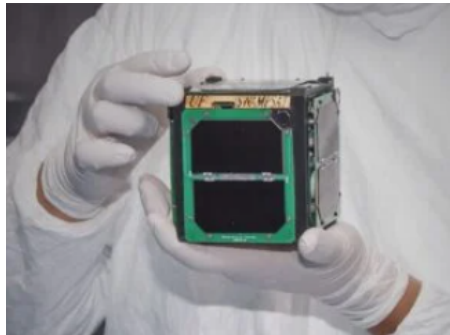


*Figure 1: First CubeSat design, illustrating the 1U configuration*

One of the most common sizes is the 3U satellite, shown among other sizes in Figure 2, which resembles 3 1U satellites stacked on top of each other, creating a rectangular prism that is 30 cm in length. While CubeSats were initially created for the niche application of a classroom setting, their low price point, highly customizable design, small physical footprint, and compatibility with commercial-off-the-shelf (COTS) components attracted non-academic interest. With their first successful launch in 2003, CubeSats' promising potential was coming to fruition.

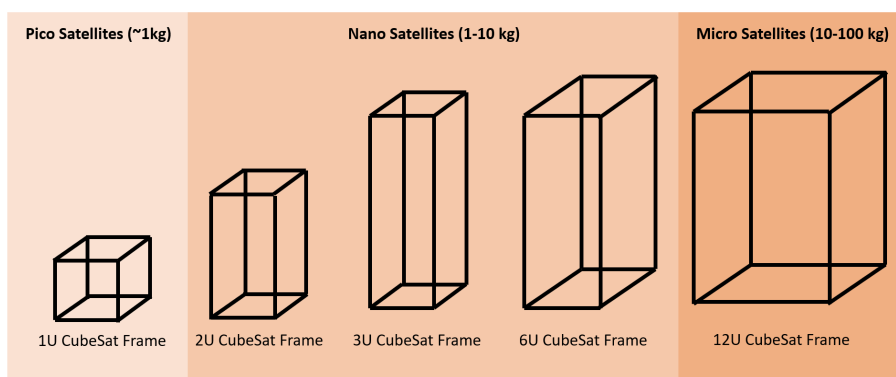


*Figure 2: CubeSat scaling, illustrating their range from pico to micro satellites (based on weight)*

## 2.2 Modern Context

In the 25 years since their creation, CubeSats have revolutionized the barrier to entry of operation in low-Earth orbit (LEO) by providing quick, cheap, lightweight vehicles that can perform well in Earth's most congested orbital regime. Technology development is pacing well with the CubeSat's space-constrained design, with miniaturization of key electronic components progressing quickly [2]. Commercial and governmental use continues to expand, with CubeSats being implemented by federal agencies like NASA and ESA and companies like Kepler Communications and Airbus [3]. A major impact of CubeSats' proliferation is the growth in satellite constellations.

Prior to CubeSats' creation, the largest satellite constellation, Iridium, consisted of 66 satellites and required an estimated \$5 billion to set up [4]. By contrast, the largest modern constellation, SpaceX's Starlink, consists of 6,370 satellites and costs an estimated \$10 billion to set up [5]. Increasing the number of satellites by two scales of magnitude with the resulting increase in cost by only a factor of two would be impossible without the technological advancement in miniaturization and mass production. Though Starlink's constellation is composed of small satellites, which are significantly larger and heavier than CubeSats, the massive constellation's existence and the growing interest in large fleets of smaller satellites places CubeSats in an advantageous position. For companies and researchers without \$10 billion to spend, constellation-reliant missions are fully achievable with CubeSat capabilities.

## 2.3 CubeSat Solar Array Designs

Given their relatively small size, CubeSats must minimize their total weight and maximize on-orbit power generation to maintain their cost-effectiveness. To satisfy both constraints, solar arrays are applied in a variety of configurations with either passive or active designs. Passive solar array configurations typically fall into two categories: body-fixed or static deployable. For a body-fixed example, refer back to Figure 1, where the solar cells are attached to the sides of the 1U CubeSat. This method doesn't can rarely satisfy as a primary power source but is useful in terms of providing auxiliary power for shorter length missions. Deployable solar arrays are similarly self-explanatory, capable of

starting from a launch configuration that fits within the standardized CubeSat launch vehicles (a.k.a. P-Pods) shown in Figure 3 and moving into a deployed position that brings panels planar to a chosen face of the satellite.

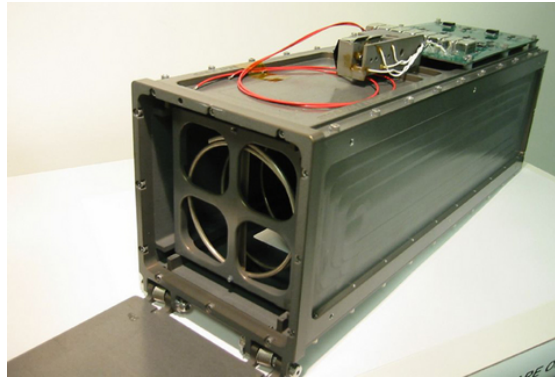


*Figure 3: Poly Picosatellite Orbital Deployer (P-POD) for up to a 3U CubeSat*

These deployable systems typically use a passive, non-reversible deployment mechanism like a spring loading and a burn wire that ignites after launch, releasing the panels to lock into place on orbit. By contrast, active systems may use motors to deploy and articulate solar arrays after launch, allowing for the panels to track with the Sun while in orbit. A single-axis system is capable of rotating about one axis, while a dual-axis system is capable of articulating with two rotational degrees of freedom. While static deployment alone provides significant improvements to the power generation of a given satellite, it's best suited to missions with regular orbits and predictable solar angles. When considering highly elliptical orbits or missions involving longer eclipse dwell times, active solar array configurations have a significant advantage with their environmental responsiveness.

## **2.4 Expected Outcomes**

When comparing the solar energy capture of all four configurations (body-fixed, deployed, single-axis, and dual-axis), it is expected that body-fixed panels will likely offer the lowest voltage output as their orientation relative to the Sun changes over time and is often suboptimal. Fixed-deployed panels, positioned at a set angle ( $90^\circ$ ), are expected to improve upon body-fixed configurations by providing more consistent exposure to sunlight, though they typically cannot match the output of the single and

dual-axis tracking systems. Single-axis systems are likely to provide better power generation than both body-fixed and fixed-deployed panels, as they adjust to maintain a more favorable solar incidence angle during the orbit. Finally, it is expected that a dual-axis configuration, capable of tracking the Sun both in pitch and yaw, will generate the highest power, as such a system attempts to maintain complete two-dimensional alignment with the Sun throughout the CubeSat's orbit.

### 3. Experimental Technique

#### 3.1 Designing the Model CubeSat

##### 3.1.1 Frame

Following the configuration of a 3U CubeSat, the initial frame dimensions were set at 10x10x30 cm. However, this design did not account for the additional size introduced by the proposed dual-axis system, primarily from the tilt axis and servo motor. Additionally, the camera responsible for locating the position of the light source required elevation to align with the system, as its field of view was partially obstructed when mounted directly on the top platform. Other small adjustments included adding another platform to hold the stepper motor driver, realigning holes to match the stepper motor, and adding more openings for wires to move across the frame.

Figure 4(a) demonstrates the initial design of the frame while Figure 4(b) shows the revised version. The dual-axis system contributed approximately 6 cm in height, leading to a reduction in the distance between the top and bottom platforms from 30 cm to 24 cm.

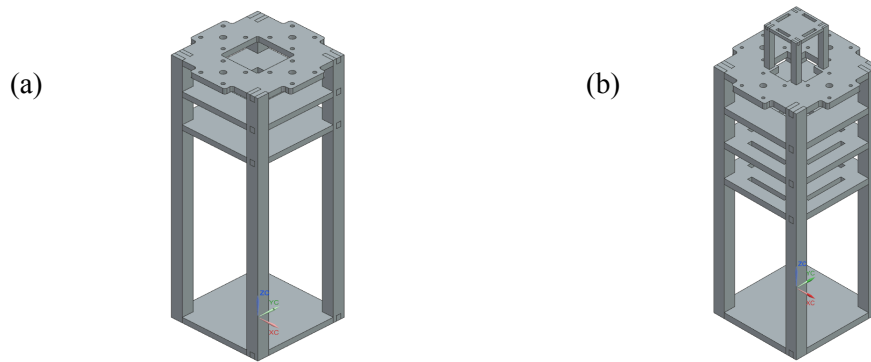


Figure 4: (a) Initial design and (b) revised version of frame assembly

While all other platforms were fixed in place, the camera tower and topmost platform on the frame were both removable. This allowed for easier electronic integration and adjustment of components during testing, which was underappreciated in the first design iteration and made troubleshooting difficult.

### 3.1.2 Dual-axis System

As the goal was to maximize the solar radiation exposure captured by the solar cells, the purpose of the dual-axis system is to actuate the side panel along the pitch and yaw axis. The dual-axis system is shown in Figure 5.

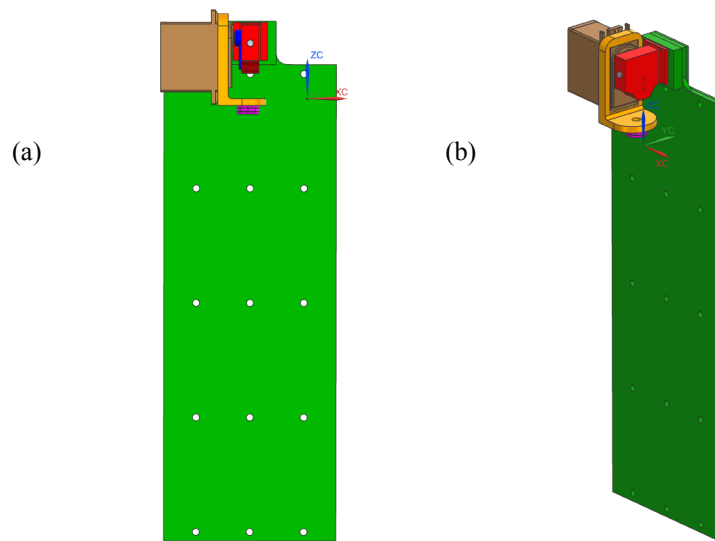


Figure 5: Isometric (a) and side (b) view of the dual-axis system

Components and their intended purpose are highlighted in Table 1. The side panel itself was designed as 10x30 cm, meaning that it would completely cover the internals of the CubeSat when in its fixed position.

Table 1: Components present in the dual-axis system

Component	Color	Purpose
Tilt Axis	Orange	Translates rotation of stepper motor in yaw axis
Servo Attachment	Red	Translates motion for pitch rotation of panel
Servo Motor	Brown	Generates rotation in the pitch axis
Servo Horn	Blue	Transfers motion to servo attachment
Thrust Bearing	Magenta	Reduces friction between tilt axis and top platform

Panel Housing	Green	Carries solar cells
---------------	-------	---------------------

Throughout the design phase of this project, three different servo motors were used, necessitating a new tilt axis for each iteration to accommodate variations in size. The servo attachment was also adjusted as the servo motor size varied to prevent collisions during panel rotation.

Figure 5 is shown without the stepper motor, as the motor is mounted directly to the frame. Nevertheless, its shaft connects to the base of the tilt axis, enabling rotation about the yaw axis. This final component completes the dual-axis system, fully enabling rotation about two axes. A combination of stepper and servo motors was chosen specifically to address size constraints. Within the CubeSat, a platform could be installed to securely house the stepper motors, with only their shafts extending outside the frame. This design minimized space usage while allowing the yaw axis, which requires precision due to its constrained range, to operate effectively.

For controlling the pitch angle, the motor needed high torque capabilities to rotate the panel reliably. Using a stepper motor for this task was not practical, as it lacked a secure mounting option and would have cluttered the upper portion of the CubeSat. The expected physical footprint of the first selected servo motor further supported this decision, as its smaller size would reduce the risk of collision while the dual-axis system operated.

### 3.1.3 CAD Assembly

Figure 6 illustrates the designed CubeSat in (a) its fixed position and (b) its deployed position. Preliminary angle limitations were set at  $0^\circ$  to  $120^\circ$  for the servo motor (pitch axis) and  $-30$  to  $30$  degrees for the stepper motor (yaw axis), ensuring optimal functionality within the spatial constraints of the CubeSat. While the servo motor was permitted to operate between  $0^\circ$  and  $120^\circ$ , this was mainly for the initial panel deployment. While testing, the servo was constrained between  $60^\circ$  and  $120^\circ$ . Some components not previously mentioned but present in this model include a Raspberry Pi Camera Module 3 Wide Angle, a Raspberry Pi, and a breadboard. The Raspberry Pi would then be connected to a monitor, keyboard, and mouse to initialize and activate the sun-tracking algorithm.

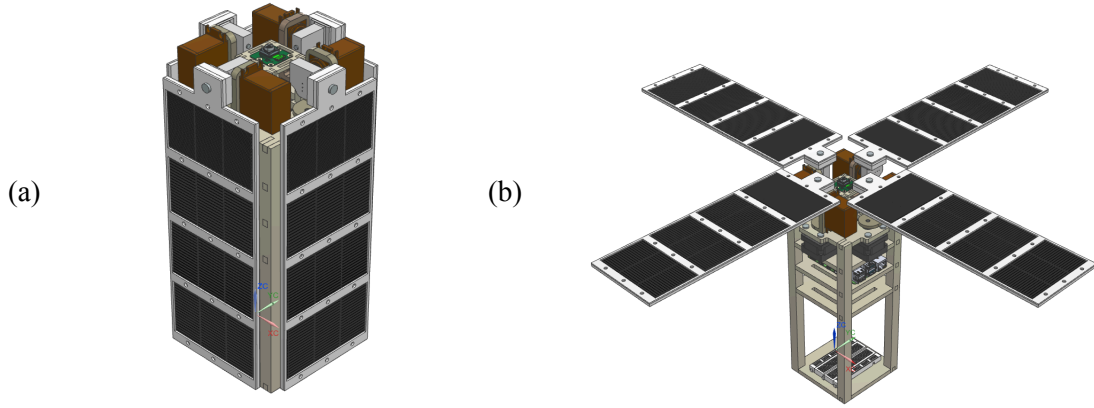


Figure 6: CAD Model of CubeSat in its (a) fixed and (b) deployed states

### 3.2 Sun-tracking Algorithm

The articulation module's sun-tracking algorithm includes both hardware and software components to compute the solar array configurations that maximize solar efficiency. Regarding hardware, a Raspberry Pi Camera Module 3 Wide Angle is used to detect visible light from the sun. The wide-angle version with a 102 degree by 67 degree field of view (FOV) was chosen to enable the algorithm to track the largest possible area overhead at any given moment.

The primary software component of the sun-tracking algorithm is the script *articulate.py* whose main function *main()* is presented in Appendix A. *main()* utilizes functionality from Python's *OpenCV* and *RPi.GPIO* libraries for sun tracking and motor actuation, respectively. A high-level overview of this algorithm is presented below in Figure 7.



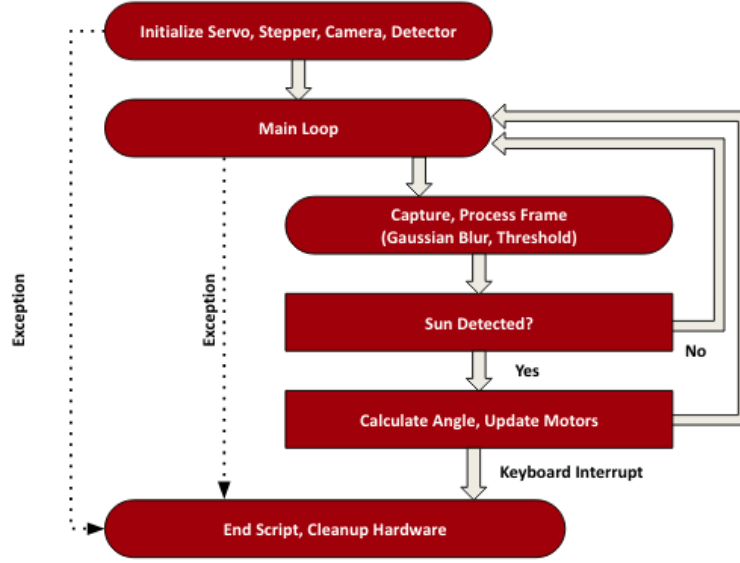


Figure 7: High-level flowchart of code and sun-tracking logic.

To track the sun and compute optimal solar array configurations, *main()* begins by initializing the motor and camera hardware. Then a *cv2.SimpleBlobDetector* object is imported such that only bright, highly circular features like the sun are detected. As *main()* runs in a loop, the detector object processes each frame, checking continuously for the presence of a light source and recording its coordinates once detected. These coordinates are used to calculate the angular deviation of each motor/panel from the optimal setpoint via the system of equations for the tilt axes (Eqn. (1a) and (2a)) and yaw axes (Eqn. (1b) and (2b)), below. It should be noted that these equations reference the opposing panel configuration presented in Figure 8(b), where the leftmost servo/stepper pair was arbitrarily designated as the primary tilt/yaw axis.

$$\theta_{pitch_1} = -\frac{\gamma_{pitch_{max}} - \gamma_{pitch_{min}}}{FOV_y} \alpha_y + \beta_{pitch} \quad (1a)$$

$$\theta_{yaw_1} = \pm \left( \frac{2\gamma_{yaw_{max}}}{FOV_x} \alpha_x + \beta_{yaw} \right) - \theta_{yaw_1}^{t-1} \quad (1b)$$

$$\theta_{pitch_2} = 180^\circ - \theta_{pitch_1} \quad (2a)$$

$$\theta_{yaw_2} = \theta_{yaw_1} \quad (2b)$$

In the above equations,  $\alpha$  is the angular position of the sun relative to the image center,  $\gamma$  is the motor/panel range limit (to avoid collisions),  $\beta$  is an offset angle,  $FOV$  is the camera field of view,  $\theta^{(t-1)}$  is the current motor/panel angle, and  $\theta$  is the optimal, solar efficiency maximizing angle. This system of equations is derived under the assumption that solar efficiency is maximized when incident light is normal to the solar panel [6].

Once  $\theta_{pitch}$  and  $\theta_{yaw}$  are calculated, all four motors are articulated toward these optimal setpoints. For testing purposes, these adjustments occur roughly every 0.8 seconds. In deployment, however, this is reducible to 1-degree adjustments every 10 seconds by simply including the line *time.sleep(10)* at the end of the main loop.

Though a more robust PID-based algorithm was initially discussed, it was discarded upon the realization that the motor position error signals necessary for PID control could not be calculated without additional hardware, like encoders. Thus, the current implementation relies primarily on dead-reckoning. To remedy the issue of error accumulation over time (which is primarily a stepper motor issue), a limit switch is used to periodically home both stepper motors to a known absolute position of  $30^\circ$ , before returning back to  $0^\circ$ .

### 3.3 Experimental Set-Up

#### 3.3.1 Building the CubeSat Replica

Initially, the objective was to test the functionality of the dual-axis system, leading to the proposal of building one panel housing. However, further discussions concluded that incorporating two panels, whether positioned adjacent to or opposite each other, would better demonstrate the capabilities of the sun-tracking algorithm.

For the solar cells, each panel design initially consisted of 12 cells. There were three rows connected in parallel and each row consisted of three cells in series. During testing, each side panel

consisted of 9 cells arranged in a configuration of three rows connected in parallel, with each row containing three cells in series. This design was chosen because it closely mimics the architecture of COTS, space-ready panels, one of which could fit across one row of three solar cells. Additionally, this combination of parallel and series connections ensures continuous voltage output, even if one cell becomes disjoint.

One cell was advertised to output a voltage of greater than 5 V when placed in full sunlight. The lowest produced output voltage from the solar cell under ambient, artificial lighting conditions is  $3.02 \pm 0.05$  V. Facing away from natural light during the day, the solar cell outputs a voltage of  $4.45 \pm 0.04$  V. Comparing the voltage output from an artificial light source (flashlight) and a natural light source (Sun), the maximum output ranges between  $6.11 \pm 0.05$  V and  $6.21 \pm 0.04$  V, respectively. Referring back to the CAD CubeSat model, Table 2 provides information on how the major components were manufactured.

Table 2: Manufactured components for CubeSat

Component	Material	Manufactured
Frame	Acrylic (1/16", 1/8", 1/2")	Laser Cut
Side Panel	Acrylic (1/16", 1/8")	Laser Cut
Tilt Axis	ABS	3D Print
Servo Attachment	ABS, Wood	3D Print, Band Saw

The frame components were designed with finger joints to simplify assembly and were secured using epoxy. All parts, except for the top platform, were glued. The ability to remove the top allowed for easy removal of the stepper motors when necessary. Similarly, the components of the side panel were bonded with epoxy. The holes across the bottom housing allowed for soldering solar cells behind it.

The tilt axis was fabricated from ABS because of its durability, as it would be subjected to substantial movements and potential heat from the motors. However, even with ABS, the hole for the stepper motor gradually deformed after extensive testing. Eventually, sudden motions by either motor

would result in the dual-axis system sliding off. This issue persisted despite modifying the stepper motor to incorporate a D-cut shaft. To mitigate the problem, the tilt axis was detached after every trial, and an extra tilt axis print was kept on hand for replacements when needed.

For the servo attachment, it was also initially 3D-printed using ABS for its strength and ability to securely hold the panel. However, due to the small size and distance between the holes of the servo horn, there was no set screw small enough to fit into the 3D-printed servo attachment. Using only wood screws also was not an option, as the motion it underwent resulted in the component cracking. Therefore, subsequent versions were crafted from wood.

Some components were not included in the original CAD model due to their design complexity or last-minute adjustments. These include the stepper motor drivers, the protective camera case, and the wiring. Of the two required stepper motor drivers, one was mounted on the platform and the other at the base of the frame. The camera case was positioned on the designated camera platform, while wires were added as needed during assembly. Figure 8 depicts the completed CubeSat, showcasing all the integrated components.

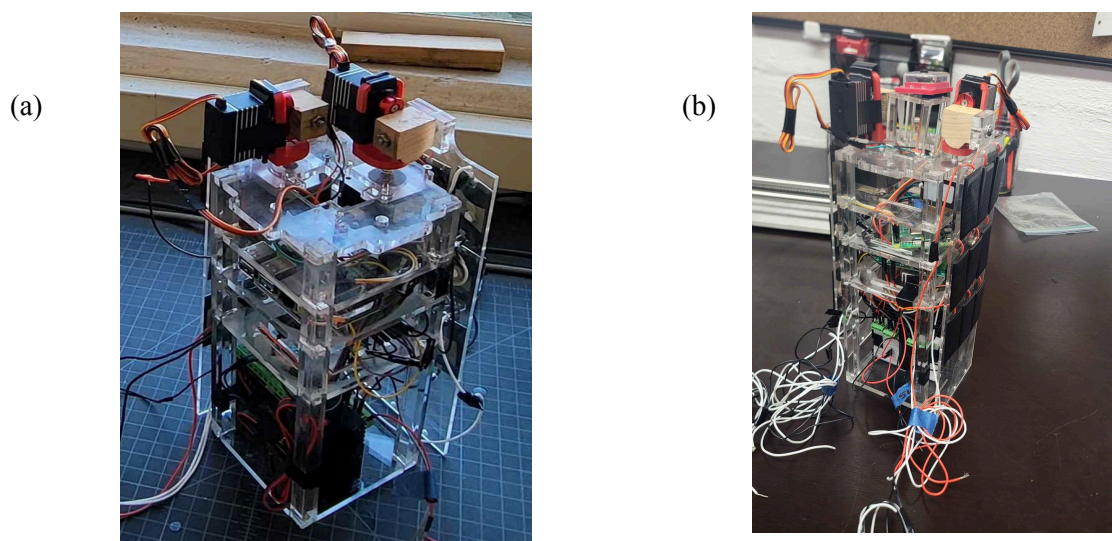


*Figure 8: Built CubeSat with panels (a) adjacent and (b) opposite*

### 3.3.2 Testing Apparatus

To evaluate the model CubeSat's articulating solar arrays, a light-controlled environment and testing apparatus were combined. The testing rig consisted of three key components: a lateral traverse, an aluminum L-Frame, and a flashlight as the light source. The lateral traverse, operated using LabView software and an attached stepper motor, produced replicable motion along a single direction. The L-Frame, constructed from 8020 and attached to the traverse using brackets, minimized the small oscillations possible as the traverse crossed from one end to the other. The flashlight was attached to the end of the L-frame, with the bulb flush with the frame's bottom. This positioned the flashlight approximately 42 cm above the infrared camera on the top face of the model, with the full CubeSat model and testing apparatus shown in Figure 9.

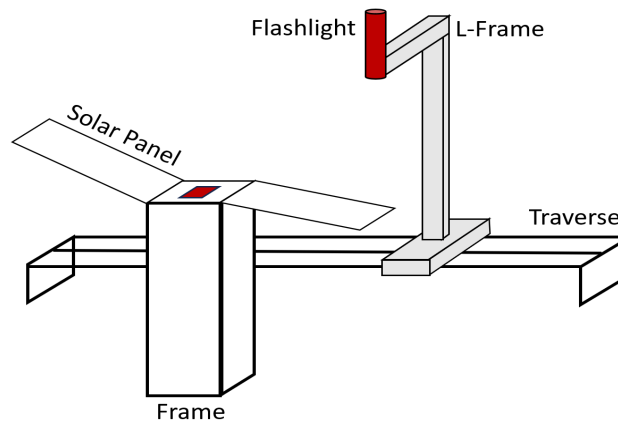


*Figure 9: Simplified experimental setup depicting the CubeSat model and testing apparatus*

## 4. Results and Discussion

As discussed in Section 3.3.1, expected voltage ranges for an artificial light source were estimated between 3.02 and 6.11 V. However, that initial range did not account for the distance between the light source and the solar cell, which was nominal during initial calibration. The voltage values were significantly lower than the expected range during experimentation since the artificial light source was positioned 42 cm from the infrared camera. The primary objective during testing, voltage output comparison between configurations, guided the decision to normalize the recorded voltage and better

illustrate performance differences. All of the following plots display normalized voltage, reducing the effects of the artificial light's variable brightness and distance from solar cells for each configuration. Each trial is defined by the CubeSat orientation at a specific angle relative to the traverse. Each set consists of three to four trials, and the maximum voltage value used for normalization is determined from the trials within that set.

Trials consisted of the CubeSat in a launch position to simulate a body-fixed configuration, panels pitched 90° from the body to simulate a static deployed configuration, operating with an inactive stepper motor to simulate a single-axis system, and operating with both motors active for a dual-axis system. Figure 6 displays a clear visualization of the CubeSat being in its fixed position and deployed position, relevant for simulating the two passive configurations. For the single-axis system, the pitch axis was chosen as the degree of freedom, as it provided a more comparable basis for evaluation.

#### 4.1 Initial Voltage Testing with Single Solar Panel

During initial testing, two-panel integration was in progress, thus only one panel was monitored for voltage output. No data for the single-axis system was recorded since the final iteration of testing ended prematurely due to issues with the traverse motor overheating. The following figures present the servo angle (top left), the stepper angle (top right), and the normalized voltage (bottom) over time. Figure 10 shows when the CubeSat is parallel (0°) relative to the traverse.

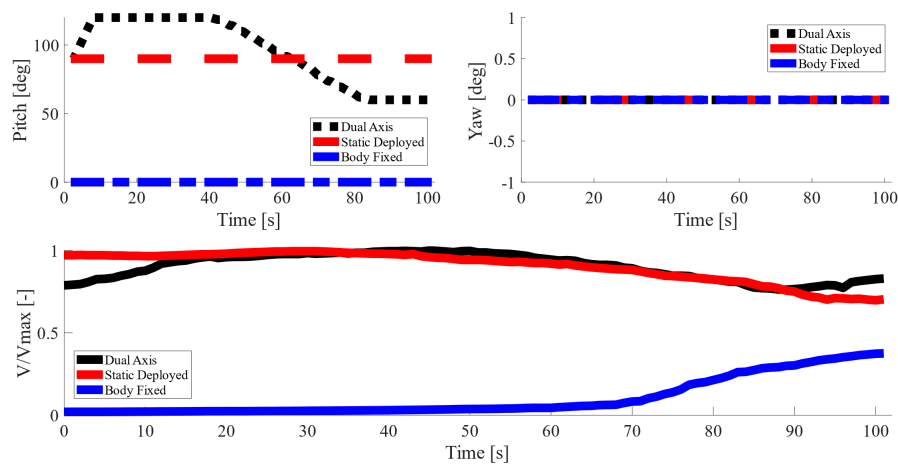


*Figure 10 : Motor angles and voltage output when parallel ( $0^\circ$ ) relative to the traverse*

The clear disparity between the two passive systems, static deployed and body-fixed, is as expected given the body-fixed configuration's reliance on ambient light instead of being able to achieve direct exposure to the light source. However, the comparable output between the static deployed and dual-axis systems was unexpected. It is also important to note that the stepper motor was not activated when testing with the dual-axis system. Since the light source was parallel to the panels, the required motion was entirely handled by the servo motors, simulating a single-axis system response. Figure 11 then shows when the CubeSat is perpendicular ( $90^\circ$ ) relative to the traverse.

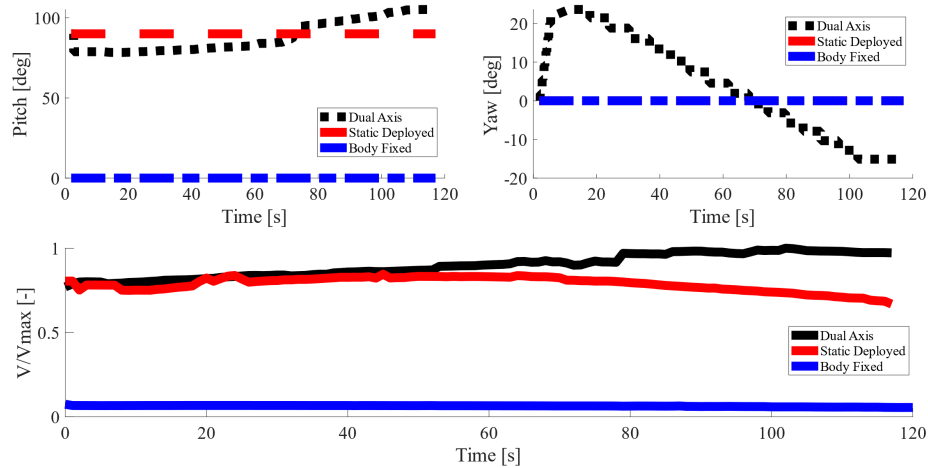


*Figure 11: Motor angles and voltage output when perpendicular ( $90^\circ$ ) relative to the traverse*

The disparity between passive systems remains evident in this configuration. However, a separation of voltage between the static deployed system and the dual-axis system is now apparent. As illustrated in the dual-axis stepper movement, the panels being perpendicular to the light source require lateral motion from left to right to achieve optimal positioning. Naturally, as the light source moves further from the center, the voltages generated by the static deployed system decrease. Table 3 shows the voltage output for each trial across both sets.

Table 3: Comparison between mean voltage output of each system based on orbital inclination

System Type	Orbital Inclination	
	0°	90°
<b>Dual-axis</b>	$4.8 \pm 0.4$ V	$3.5 \pm 0.3$ V
<b>Deployed</b>	$4.8 \pm 0.5$ V	$3.1 \pm 0.2$ V
<b>Fixed</b>	$0.5 \pm 0.5$ V	$0.25 \pm 0.02$ V

The table above highlights how well the deployed system is performing, generating voltage levels comparable to those of the proposed dual-axis system.

#### 4.2 Dual Panel Testing

This round of testing marked the first incorporation of the second panel. The same three configurations—both passive and dual-axis articulated—were evaluated. Figures 12 and 13 display the voltage output of the solar cells when positioned at 80° and 60° relative to the traverse.

For the dual-axis system, it is important to note that the stepper motion was synchronized for both panels to prevent collisions with other hardware. Instead of the traditional angles of 0°, 45°, or 90°, angles of 60° and 80° were chosen to showcase a unique configuration and assess the dual-axis system's performance under these conditions. In this setup, a significant disparity between voltage output from the panels of the same system was observed, indicating that the algorithm was primarily focused on optimizing the orientation of a single panel. This result highlights areas for potential improvement in balancing performance across both panels.

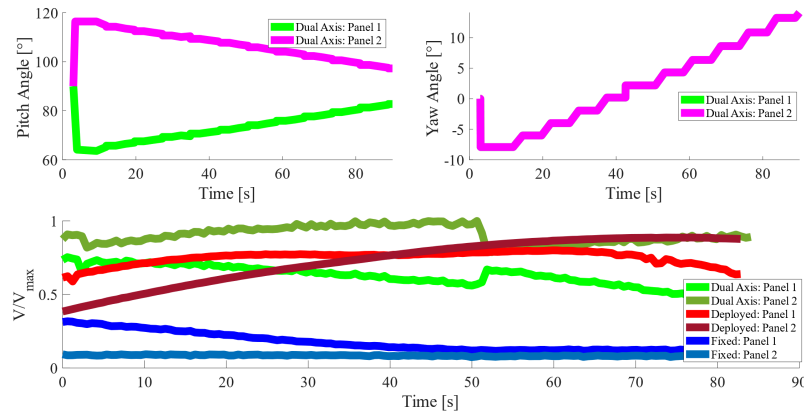


Figure 12: Orbital inclination and voltage output at 60° relative to the traverse



Similar to Figure 12, the panels vary in output when oriented  $80^\circ$  from the traverse. Following the performance trend observed in earlier tests, the body-fixed configuration displayed the poorest performance. The dual axis system demonstrated initial superior performance to the two passive systems, but tracks equal to or lesser than voltage output to the static deployed system as the light passes the midpoint of the span. The static deployed system output never reaches the maximum normalized value achieved by the dual axis system, but performed predictably with tapering on the beginning and end of the span where the least surface area was covered by direct overhead light.

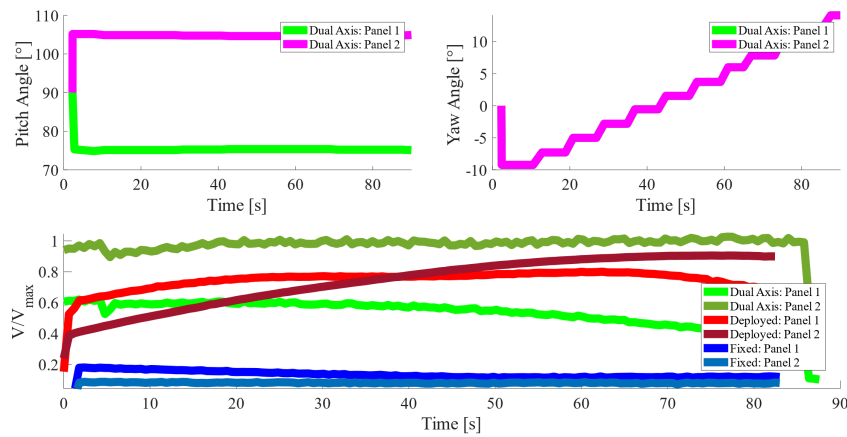


Figure 13: Orbital inclination and voltage output at  $80^\circ$  relative to the traverse

While the disparity between Panel 1 and Panel 2 is evident, the algorithm did not sacrifice consistency. Throughout the trials, the voltage output remains stable, with no significant fluctuations. This consistency is further detailed in Table 4.

Table 4: Comparison between mean voltage output of each system based on orbital inclination

System Type	Orbital Inclination	
	$60^\circ$	$80^\circ$
<b>Dual-axis</b>	$1.9 \pm 0.2$ V	$1.8 \pm 0.2$ V
<b>Deployed</b>	$0.95 \pm 0.3$ V	$1.08 \pm 0.3$ V
<b>Fixed</b>	$0.32 \pm 0.08$ V	$0.26 \pm 0.05$ V

### 4.3 Final Round of Testing

Continuing to operate with both panels, with an updated algorithm, all 4 systems were tested.

Figure 14 is when the CubeSat is positioned parallel ( $0^\circ$ ) to the traverse.

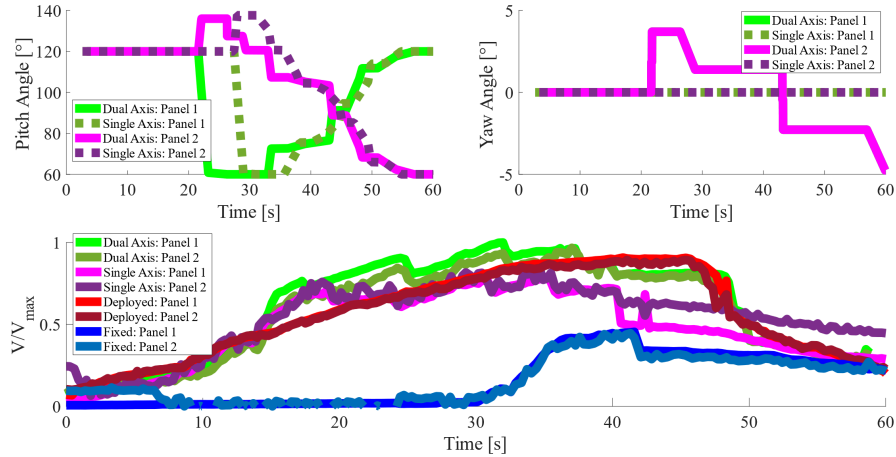


Figure 14: Motor angles and voltage output when parallel ( $0^\circ$ ) relative to the traverse

Here, the disparity between Panel 1 and Panel 2 across all systems is remarkably low. For the dual-axis system in particular, this consistency serves as a strong indicator that the algorithm is functioning as intended. As noted in Section 4.1, the CubeSat in a parallel configuration should not utilize the stepper motors. However, in this case, both stepper motors in the dual-axis system exhibit motion, likely caused by the abrupt movements of the servo motor. Given the objective of achieving high and consistent voltage across the entire trial, the dual-axis system excels in both aspects, demonstrating its effectiveness compared to other systems. Figure 15 shows when the CubeSat is angled  $45^\circ$  relative to the traverse.

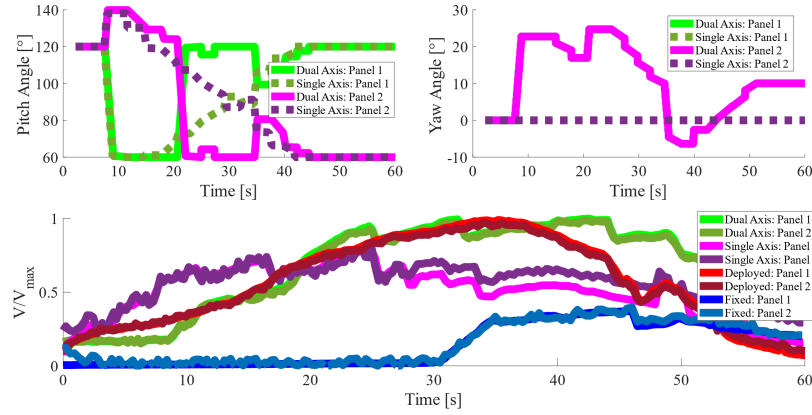


Figure 15: Motor angles and voltage output when angled 45° relative to the traverse

This trend of consistency is even more evident in this configuration. Comparing the dual-axis and deployed systems, the deployed system exhibits a voltage profile resembling a parabola, while the dual-axis system displays a profile more akin to a top hat. This distinction is significant, as it indicates that the deployed system achieves peak performance only for a brief period, whereas the dual-axis system continuously adjusts to maintain optimal light exposure, resulting in a more consistent voltage output. Figure 16 shows when the CubeSat is positioned perpendicular (90°) to the traverse.

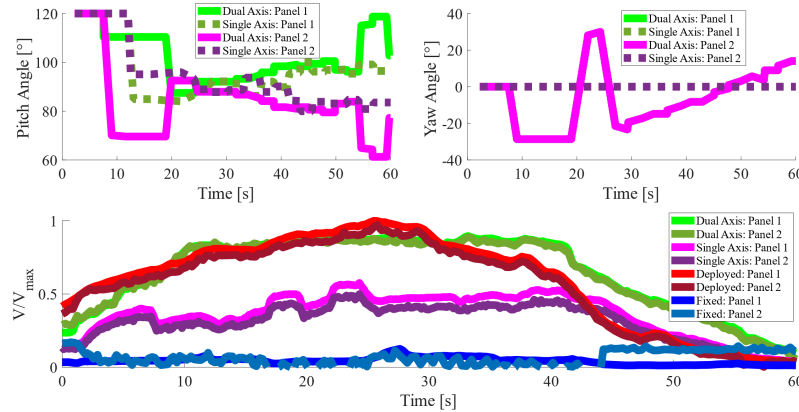


Figure 16: Motor angles and voltage output when perpendicular (90°) relative to the traverse

When the panels are perpendicular to the light source, the deployed configuration remains the primary competitor to the dual-axis system. While the deployed configuration occasionally peaks slightly

higher than either of the dual-axis panels, its voltage output declines at a much steeper rate. Table 5 summarizes the average voltage output for each system across all sets.

Table 5: Comparison between mean voltage output of each system based on orbital inclination

System Type	Orbital Inclination		
	90°	45°	0°
<b>Dual-axis</b>	$3 \pm 1 \text{ V}$	$3 \pm 1 \text{ V}$	$3 \pm 1 \text{ V}$
<b>Single Axis</b>	$1.5 \pm 0.6 \text{ V}$	$2.5 \pm 0.7 \text{ V}$	$2.4 \pm 0.8 \text{ V}$
<b>Deployed</b>	$2.9 \pm 0.9 \text{ V}$	$2.6 \pm 1 \text{ V}$	$3 \pm 1 \text{ V}$
<b>Fixed</b>	$0.2 \pm 0.1 \text{ V}$	$0.6 \pm 0.5 \text{ V}$	$0.7 \pm 0.6 \text{ V}$

#### 4.4 Design Challenges

The CubeSat Dual-Axis Solar Array Articulation experiment faced several challenges during its design, testing, and data collection phases, which led to several limitations and areas for improvement. These issues affected the system's performance and the quality of the results, but also provided valuable insights into the functioning of the solar array articulation system.

One of the primary issues encountered was the looseness of the screws on the servo attachment. This caused the solar panel to experience significant slack during operation, leading to inaccurate positioning of the panel. Such misalignment resulted in suboptimal power generation in certain configurations, particularly when the panel failed to maintain proper orientation with the light source. This problem could have been mitigated by ensuring a more secure attachment and possibly using stronger or more durable fasteners to prevent movement over time.

In the first dataset, the holding current for the stepper motor was not properly set up, causing the panels to move freely along their yaw axis. This lack of restraint was initially overlooked due to overheating issues when attempting to apply a holding current. The absence of a reliable hold on the panels contributed to poor alignment and inconsistent voltage output during the first trials. It would be beneficial to optimize the motor control settings and perhaps use a cooling system to prevent overheating, which could allow for consistent holding current application.

Another issue arose with the design of the camera platform, which was sized for the initial smaller servo selection and would collide with the larger servo motor selected to ensure sufficient holding torque. This design flaw necessitated the removal of the platform during data collection to prevent interference with the stepper motor's movement. The camera's position and stability are crucial for effective sun-tracking, and this issue could be resolved by redesigning the camera platform to accommodate the larger servo without obstructing other components.

The tilt axis, which was connected to the stepper motor, also posed problems during testing. It frequently slid off the shaft of the stepper, causing inconsistent motion and interruptions in data collection. This issue, although partially mitigated by temporarily detaching the tilt axis after each trial, hampered the experiment's progress. Future designs could use more robust fastening methods or reinforce the tilt axis component against wear and heat-related deformation to prevent slippage during movement.

A more unexpected issue was the failure of the stepper motor on the traverse, which halted the system's ability to move the light source for proper testing. To continue, a team member had to manually hold and move the flashlight. This failure could have been avoided by ensuring the stepper motor was properly calibrated and its electrical connections securely fastened. Moreover, the traverse length was too small for the camera to utilize its full FOV, which limited the camera's ability to accurately track the light source. Extending the traverse length or adjusting the camera's FOV to better accommodate the available space would enhance the system's ability to track the sun efficiently.

Another issue encountered during testing were the continuous experimental design changes that necessitated frequent updates to the tracking algorithm. Without adequate testing between each of these design changes, bugs such as the lower servo limit not being obeyed, affected portions of the data collection until they were identified and resolved.

During testing, the goal was to reduce the disparity in performance between panel 1 and panel 2. However, several factors, including inconsistent motor movement and occasional servo motion interference with the stepper, resulted in suboptimal alignment and voltage output. Despite these setbacks, the light source performed better than expected, as its proximity to the panels improved the voltage output

in most cases. However, the panels did not produce the expected voltage levels in certain configurations, likely due to the aforementioned mechanical issues and suboptimal alignment. In the final dataset, the servo motion occasionally caused unintended movement in the stepper motors, as observed when the panel reached 90 degrees. This interference, possibly due to mechanical coupling or insufficient isolation between the servo and stepper motors, led to further inaccuracies in panel positioning. Addressing this issue by improving the mechanical decoupling between the motors or using more advanced motor controllers could prevent such unintended movements in future experiments.

While the dual-axis articulation system showed promise and outperformed passive configurations in certain trials, the various issues faced during testing hindered the system's ability to achieve optimal performance. The results underscore the need for careful consideration of component compatibility, motor control, and structural integrity in the design of such systems. Future iterations will benefit from addressing these issues, particularly focusing on motor control, structural design, and algorithm refinement to achieve more consistent and reliable solar array articulation.

## **5. Conclusion**

As mentioned in Section 4, the expected performance disparity between single and dual-axis articulation was achieved. However, the flawed testing mechanism advantaged the static deployed configuration and produced voltage outputs that were much higher than predicted. Since the linear motion of the traverse and overhead artificial light were relatively simplistic, the static deployed system undermined the usefulness of the articulation system. This is especially prominent in Figures 14-16, where despite full dual-panel integration, optimal control system performance, and maximized FOV coverage for the artificial light's motion, the static deployed system's normalized voltage directly competes and at times exceeds the dual-axis output. Similarly, the dual-axis system average voltage output typically exceeds or is functionally equivalent to the static deployed configuration, as seen in Tables 3-5.

Had more complex analysis of power generation using both voltage and current recordings been possible, perhaps the more consistent voltage output of the dual-axis system over time could have demonstrated distinct improvement over the static deployed system. Additionally, a more complex light trajectory may have demonstrated additional advantages for both articulated systems. The applied testing mechanism had predictable sun incidence angles that are best suited to the static deployed system, as discussed in Section 2, thus two-dimensional motion of the artificial light may prove useful in identifying performance enhancements in line with predictions.

The primary intent of this experiment was to demonstrate the superiority of the dual axis articulation system over a single axis articulation system, with supporting data demonstrating weaker performance from the passive configurations. While the static deployed system performed well beyond the predicted voltage output, all three other configurations performed as expected, with distinct performance improvements observed as complexity increased. By expanding the scope of test analysis to include two panels in opposite positions and recalibrating the controls to minimize the difference in output between panels, further evidence solidified the superior performance of the dual axis system over the single axis system and body fixed configuration.

This initial prototype delivers promising results across various configurations, regardless of orbital inclination. Compared to current CubeSat designs that employ a single-axis system, the dual-axis system achieves a substantial increase in voltage generation, with an improvement of  $42 \pm 7\%$ .

## 6. References (1 page, single-spaced)

1. Shubber, K., "Constellations of CubeSats are revolutionizing how we use satellites," Wired, 17 Sep. 2017 <https://www.wired.com/story/viva-los-cubesats/>
2. Yurechko, J. "Building mission success with miniaturized satellite technology," Spire, Feb. 2022 <https://spire.com/blog/federal/building-mission-success-with-miniaturized-satellite-technology/>
3. cubesat.org "Components," 2022 <https://www.cubesat.org/descriptions>
4. Graham, W. "Iridium NEXT-5 satellites ride to orbit on SpaceX Falcon 9," NASA Space Flight, 29 Mar. 2018  
<https://www.nasaspaceflight.com/2018/03/iridium-next-5-satellites-spacex-falcon-9/>
5. Baylor, M. "With Block 5, SpaceX to increase launch cadence and lower prices," NASA Space Flight, 17 May 2018  
<https://www.nasaspaceflight.com/2018/05/block-5-spacex-increase-launch-cadence-lower-prices/>
6. CE Bright Futures. "Incident Angle of Sunlight." [Online resource](#), accessed Dec. 10, 2024.



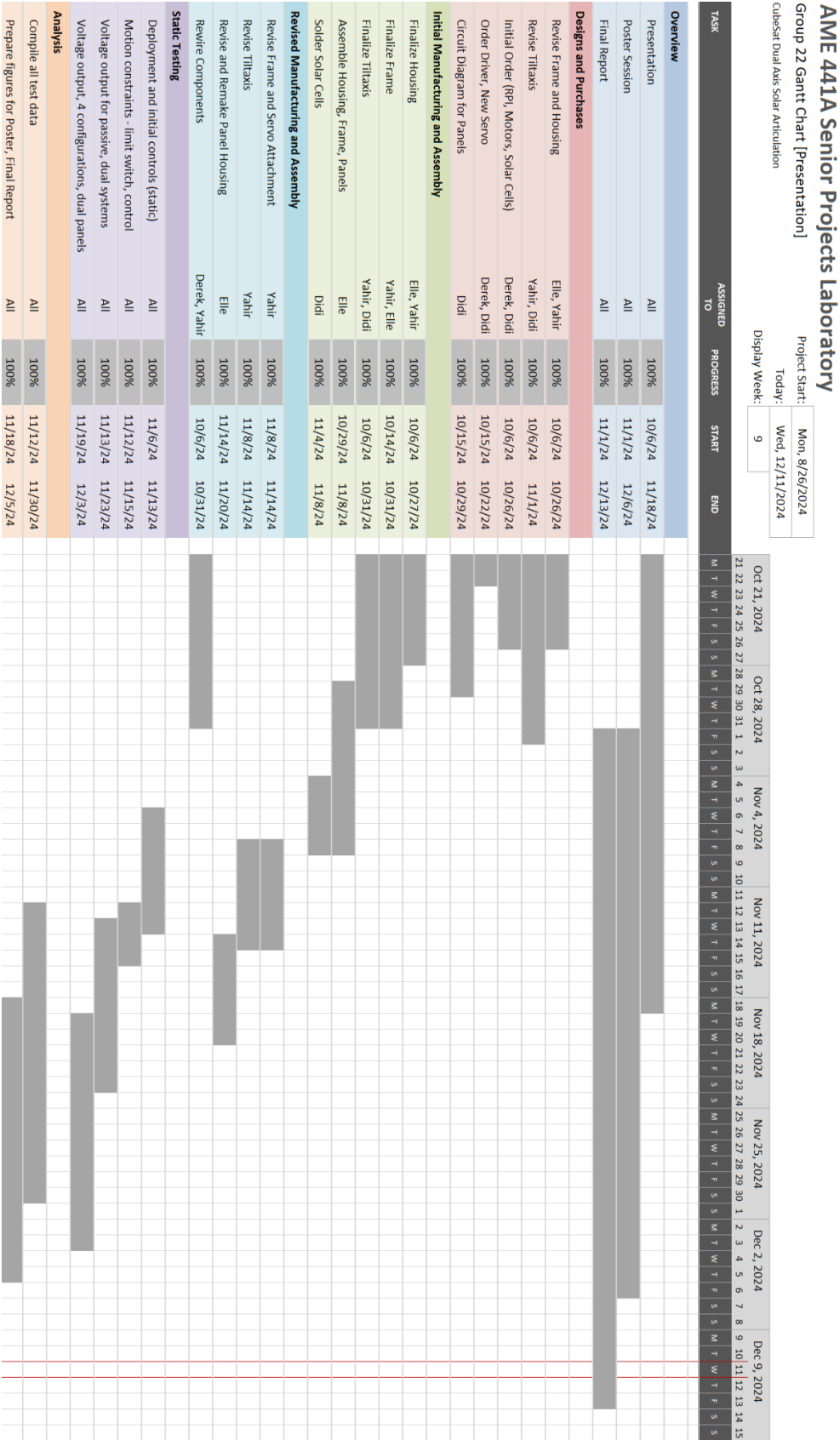
## 7. Appendix

### Appendix A

The following shows the truncated version of the function main() from articulate.py.

```
def main():
    detector = CLINGINIT.detector
    motors = initializeMotors().values()
    servo1, stepper1, servo2, stepper2 = motors
    for motor in motors:
        motor.deploy()
    camera = initializeCamera()
    start_time = time.time()
    try:
        with ThreadPoolExecutor(max_workers=4) as executor:
            while True:
                sorted_keypoints, keypoints_frame = processFrame(camera, detector)
                threads = None
                if sorted_keypoints:
                    sun = sorted_keypoints[0]
                    sunX, sunY = sun.pt
                    sunXNorm = sunX - VIEWPORT_WIDTH_MIDPOINT
                    sunYNorm = sunY - VIEWPORT_HEIGHT_MIDPOINT
                    setpoints = calculateSetpoints(sunXNorm, sunYNorm, stepper1, stepper2)
                    threads = [executor.submit(motor.move, setpoint) for (motor, setpoint) in zip(motors,
setpoints)]
                    if checkAngleChangeThreshold(motor, setpoint)]
                    elapsed_time = time.time() - start_time
                    recordMotorData(threads=threads, motors=motors, t=start_time if threads else elapsed_time)
                    print(f'time: {elapsed_time}, servo1.curr_angle: {servo1.curr_angle: .5f}, stepper1.curr_angle:
{stepper1.curr_angle: .5f}, servo2.curr_angle: {servo2.curr_angle: .5f}, stepper2.curr_angle:
{stepper2.curr_angle: .5f}")
                    cv.imshow("keypoints_frame", keypoints_frame)
                    if cv.waitKey(1) == 32:
                        break
            except Exception as e:
                print(f'An error occurred: {e}')
                raise e
    finally:
        if 'camera' in locals():
            camera.stop()
        cv.destroyAllWindows()
        for motor in reversed(motors):
            motor.cleanup()
```

Appendix B - Gantt Chart



### Appendix C - Updated Budget

Table A.1 outlines all the items purchased and used to complete this project. Notably, the project exceeded the allotted budget of \$400, primarily due to accidentally frying the Raspberry Pi. This necessitated the purchase of a replacement Raspberry Pi, a camera module, and a memory card.

Some items, although purchased, were never utilized due to design changes or alternative solutions. For example, the standoffs were rendered unnecessary by design modification, and the DC-DC buck converter was not used because the power supply was equipped with multiple channels. Additionally, the plastic servo arms were replaced by a metal servo arm found in the lab.

Table A.1: Components used and bought throughout this project

Items Available in Lab				
Items	Model	Qty	Unit Price	Item Price
Acrylic Sheets	1/16", 1/8", 1/4" thickness	6	~\$55.00	\$55.00
Limit Switches	N/A	2	\$2.50	\$5.00
Power Supply	N/A	1	~\$500.00	\$500.00
Monitor	N/A	1	N/A	N/A
Manufacturing Costs				
3D Printing (ABS)	N/A	N/A	\$1.00/in <sup>3</sup>	~\$2.00
Laser Cutting	N/A	N/A	\$40/hr	\$40.00
Items Required to Purchase				
Solar Cells	AOSHIKE 10 pc 5V 30 mA Mini Solar Panels	2	\$15.99	\$31.98
Servo Motor	MG995	2	\$4.75	\$9.50
Stepper Motor	Nema 17-39	1	\$78.64	\$78.64
Stepper Motor	Nema 17 Short Body	1	\$11.99	\$11.99
Infrared Camera	Raspberry Pi Camera Module 3 NoIR	2	\$35.00	\$70.00
Raspberry Pi 4	Raspberry Pi 4 Model B - 8 GB RAM	2	\$75.00	\$150.00
Control Power Supply	Raspberry Pi Power Supply 5.1V 3A with USB C	1	\$7.95	\$7.95

Standoffs	320 Piece M2 Male Female Hex Brass Standoffs	1	\$12.99	\$12.99
MicroHDMI-HDMI Cable	Raspberry Pi Official MiroHDMI to HDMI cable	1	\$5.95	\$5.95
64 GB Memory Card	SanDisk Pre-Installed NOOBS MicroSD Cards	2	\$19.95	\$39.90
Thrust Ball Bearings	6655K72	1	\$5.10	\$5.10
DC-DC Buck Converter	LM2596S DC-DC Buck Converter	1	\$12.99	\$12.99
Plastic Servo Arms	Plastic Servo Arms 23T Blue, 3mm Hole Single/Double Arm for JR 1 Set	1	\$9.99	\$9.99
				<i>Subtotal: \$446.98</i>
\$100 per student (4 students)				<i>Total Budget: \$400</i>
				<i>Available Budget: -\$46.98</i>

#### Appendix D - Requisite Torque Recalculation

Throughout this project, three different servo motors were used, primarily due to an initial underestimation of the required torque to rotate the panel. Below is a rough calculation of the torque needed to both rotate the panel and hold it securely in place.

Panel Housing Weight:  $w_1 = 107 \text{ g}$

Solar Cell Weight:  $w_2 = 5 \text{ g}$

Total Weight:  $w = w_1 + 12w_2 = 167 \text{ g}$

Taking the maximum length of the panel housing to provide a maximum torque estimate and rounding the total weight to 200 g:

- Force =  $0.2 \text{ kg} * 9.81 \text{ m/s}^2 = 1.962 \text{ N}$
- Torque =  $0.2 \text{ kg} * 30 \text{ cm} = 6 \text{ kg-cm}$

Taking the CAD center of mass' distance from the attaching hole (13.81 cm)\*:

- Torque =  $0.2 \text{ kg} * 13.81 \text{ cm} = 2.76 \text{ kg-cm}$

\*Neglects impact of solar cells on centroid since they are sufficiently uniformly distributed

## Appendix E - Circuit Diagram

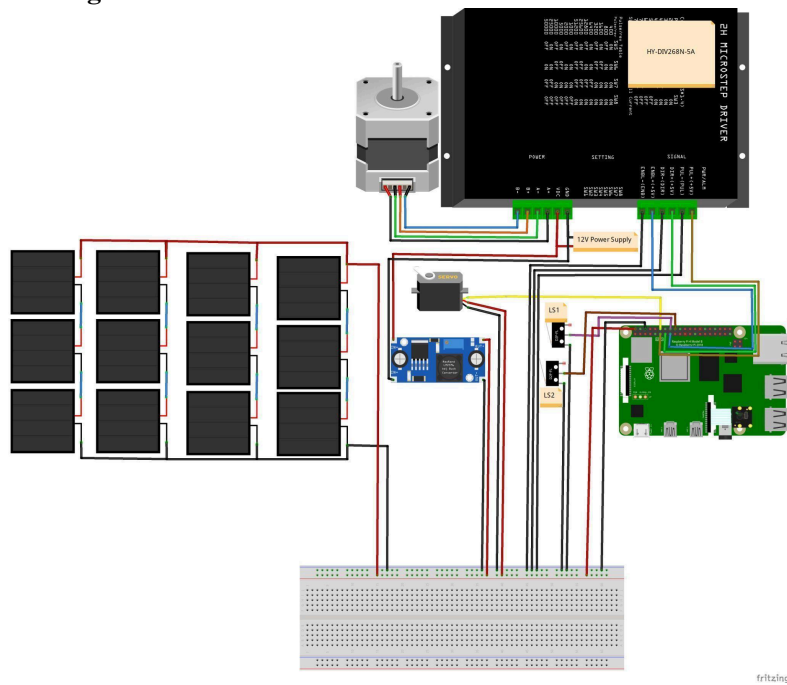


Figure A.1- Complete circuit diagram of servo motor, stepper motor, solar cells, power supply and Raspberry Pi